Magnetic flux rotation and associated magnetization peak in $La_{1.85}Sr_{0.15}CuO_4$ crystals under tilted fields

Y. Bruckental, A. Shaulov, and Y. Yeshurun
Institute of Superconductivity, Department of Physics, Bar-Ilan University, Ramat-Gan 52900, Israel
(Received 2 March 2006; published 6 June 2006)

The magnetization vector in $La_{1.85}Sr_{0.15}CuO_4$ was measured as a function of magnetic field, temperature and time for fields tilted from the *ab* plane. For small tilting angles, the magnetization amplitude curves exhibit an additional peak in between the well-known first and second magnetization peaks. Assessment of the induction vector as a function of field reveals flux rotation from the *ab* plane towards the direction of the external field, beginning at the onset of the additional magnetization peak. This flux rotation causes a tilt of the current flow plane towards an "easy" direction, namely, the *ab* plane. The additional peak results from a competition between the current increase associated with this tilt and the intrinsic current decrease associated with the field increase.

DOI: 10.1103/PhysRevB.73.214504 PACS number(s): 74.25.Ha, 75.30.Gw, 74.25.Qt

I. INTRODUCTION

Magnetic anisotropy in high-temperature superconductors has been the subject of many experimental[1–13] and theoretical[14–23] studies. These studies have revealed a range of new phenomena that could not be merely attributed to the anisotropy in the electronic effective mass. For example, a variety of new vortex phases were predicted[15–19,21–23] and observed[5,6,8,9,11–13] when the direction of the external field deviates from the principal crystallographic axes. These include the "kinked" vortex state, where vortices consist of segments of Josephson vortices connected by Abrikosov pancakes,[21] and the crossing lattices state,[15,18,21–23] where a lattice of Abrikosov vortices, along the *c* direction, coexists with a lattice of Josephson vortices running parallel to the *ab* plane. The interaction between the crossing lattices creates additional vortex states such as the chain state and the mixed chain-lattice state.[6,22,23] A unique magnetic behavior in tilted fields is also manifested in the so-called "lock-in" phenomenon[16] observed when a small external field is applied at a small angle θ_H to the *ab* planes. It was predicted theoretically[16,21] and observed experimentally[3,24–26] that there is a finite lock-in angle θ_0, such that when $\theta_H < \theta_0$, the flux lines run parallel to the planes, remaining "locked in" between the layers. Tilted fields also give rise to unique magnetization curves.[7,10,12,27] For example, multiple-peak structures were recently observed in the magnetization loops of $Bi_2Sr_2CaCu_2O_{8+y}$ and attributed to phase transitions in the two-component vortex matter composed of pancake and Josephson vortices.[7,10] Similarly, an additional magnetization peak (AMP) was observed[27] in underdoped $La_{2-x}Sr_xCuO_4$ (LSCO) crystals ($x=0.05-0.09$) in between the well known first and second magnetization peaks. This AMP was attributed to initial flux trapping in the *ab* plane, followed by flux rotation towards the direction of the external field as the field increases.[27]

In this work we examine the additional peak phenomenon in an optimally doped LSCO ($x=0.15$), and investigate, in detail, its relationship to the flux trapping and rotation effects. Our study shows that flux trapping and rotation alone cannot explain the data, and one must consider a tilt of the current flow plane associated with the flux rotation. A competition between the current increase associated with this tilt and the intrinsic current decrease due to the field increase creates the additional magnetization peak. The present study is further extended by examining the correlation between the flux rotation and the additional magnetization peak, as a function of the tilting angle and temperature.

II. EXPERIMENTAL

Parallelepiped shaped samples with dimensions $0.193 \times 0.122 \times 0.072$ cm^3 were cut from a single crystal of optimally doped $La_{1.85}S_{0.15}CuO_4$ ($T_c=38$ K), grown by the traveling-solvent-floating-zone method.[28] Using a Quantum Design MPMS-5S SQUID magnetometer, equipped with a horizontal rotator, the magnetization components M_L and M_T parallel and perpendicular to $\vec{H}$, respectively, were measured as a function of the external field $\vec{H}$, for fields applied at different angles θ_H relative to the *ab* plane. Measurements of the longitudinal and transverse components of the magnetization enable us to determine the magnitude and direction of the vectors $\vec{M}$ and $\vec{B}$. A schematic representation of the external magnetic field $\vec{H}$ and the induction $\vec{B}$ relative to the sample is shown in Fig. 1.

Measurements were performed after cooling the sample to the target temperature with no external field [zero field cool-

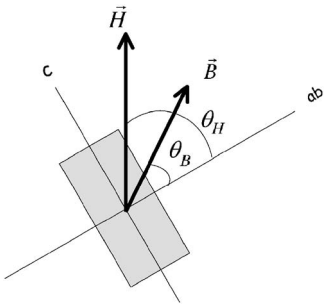

FIG. 1. Schematic representation of the external magnetic field $\vec{H}$ and the induction $\vec{B}$ relative to the sample crystallographic axes.

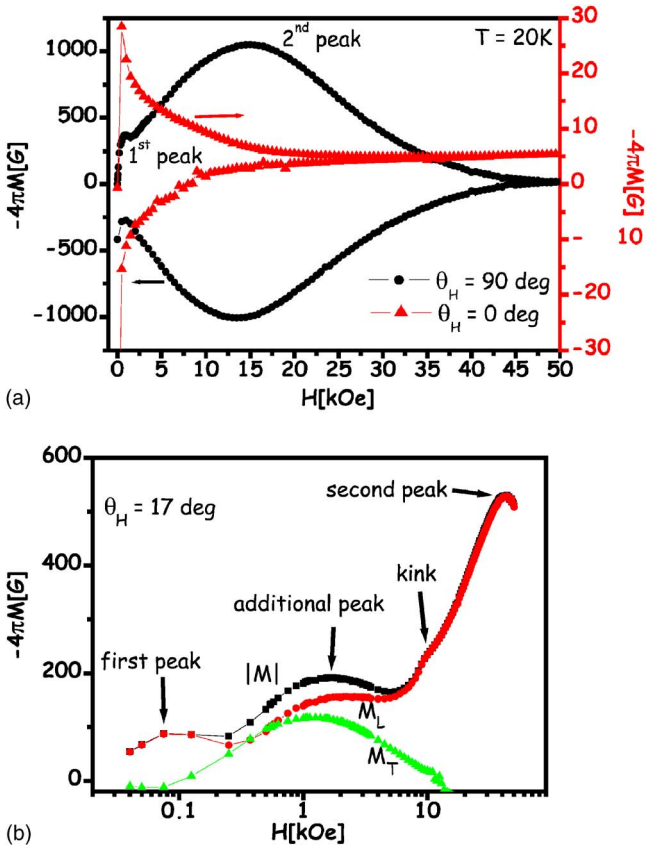

FIG. 2. (Color online) (a) Magnetization curves measured at 20 K in fields applied parallel to the c axis (circles) and parallel to the ab plane (triangles). (b) Semilog plots of the magnitude, transverse and longitudinal components of $\vec{M}$ measured at 20 K in field tilted at θ_H=17° to the ab plane.

ing (ZFC)]. The external field was swept from 0 up to 50 kOe and back down to zero in steps of 500 Oe. Magnetic relaxation measurements were performed by taking 30 consecutive measurements of magnetization in time interval of 60 s between measurements at different constant fields after ZFC procedure.

III. RESULTS

Figure 2 presents magnetization curves measured at 20 K in fields applied along principal axes and along an oblique direction, illustrating the unique difference between them. The magnetization curves shown in Fig. 2(a) were measured in fields applied parallel to the c axis (circles) and parallel to the ab plane (triangles).[29] For $\vec{H}\|c$, the conventional first and second magnetization peaks are observed, whereas for $\vec{H}\|ab$ only the first peak is observed and the second magnetization peak (SMP) is absent in the measurement field range 0–50 kOe.[30] Qualitatively different results are obtained when the applied field is not parallel to a principal axis. In this case, due to anisotropy, $\vec{M}$ is not necessarily parallel to $\vec{H}$, and both the longitudinal and transverse components of the magnetization should be measured in order to determine

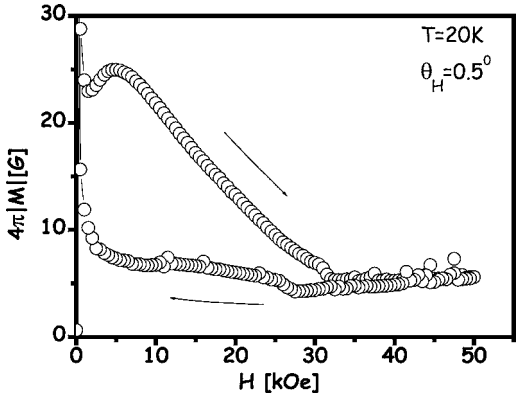

FIG. 3. Magnetization curve measured at 20 K in fields tilted at θ_H=0.5° to the ab plane, demonstrating a clear peak at the ascending branch but a very shallow peak is descending branch.

$\vec{M}$. Figure 2(b) is a semilog plot of the two components of $\vec{M}$ together with Mmeasured in field tilted at θ_H=17° to the ab plane. It is seen that in addition to the conventional first and second peaks, characterizing the magnetization curves for $\vec{H}\|c$, an additional magnetization peak appears in M in between the first peak and the onset of the second peak. Note that the transverse component of $\vec{M}$ is most significant only in the field range of the additional peak, causing a large deviation of $\vec{M}$ from the direction of $\vec{H}$. Outside this range, M_T approaches zero, and $\vec{M}$ is basically parallel to $\vec{H}$. It is interesting to note that in the descending branch of the magnetization loop lower values of M_T are measured, giving rise to a hardly noticeable, shallow AMP (see Fig. 3).

Figure 4 shows the magnitude of the magnetization vector as a function of field for fields applied at different tilting angles θ_H. It is seen that as θ_H increases, the additional peak shifts towards lower fields, becoming less and less pronounced. For θ_H near 35° the AMP merges with the first peak. The temperature dependence of the AMP is illustrated in Fig. 5, which depicts the AMP at a constant tilting angle θ_H=12°, for different temperatures. One can see that as the

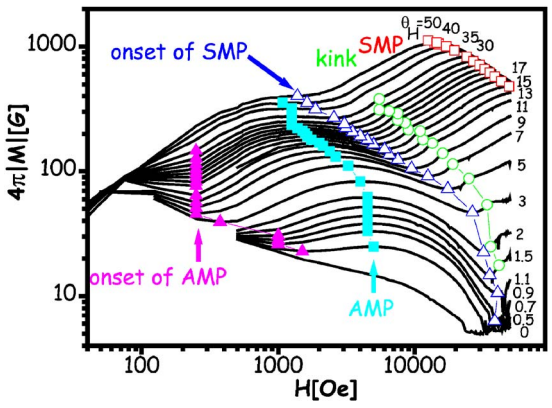

FIG. 4. (Color online) Magnitude of the magnetization vector as a function of field measured at 20 K in fields applied at different tilting angles θ_H. Characteristic features are marked: onset of AMP (closed triangles), AMP (closed squares), onset of SMP (open triangles), kink (open circles), and SMP (open squares).

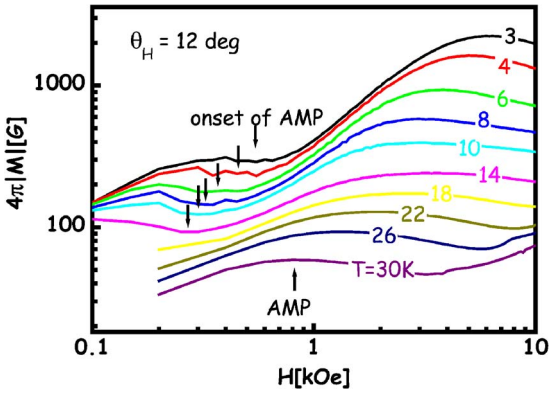

FIG. 5. (Color online) AMP at a constant tilting angle $\theta_H=12°$, measured at different temperatures. An arrow marks onset of the AMP.

temperature increases, the AMP shifts monotonically to lower fields and its height decreases.

The AMP appears in the irreversible regime of the magnetization curve, and thus it is expected to be time dependent. Figure 6 shows M vs H curves measured as follows: After ZFC the sample to $T=25$ K, the field was raised to the target field. At each step, the time dependence of the magnetization was measured during 40 min. The solid lines in Fig. 6, connect $M(H)$ data points measured at the shortest (30 s) and the longest (40 m) time. The figure shows that the AMP and its onset (see inset to Fig. 6) shift slowly with time towards lower fields.

Knowledge of the magnetization vector $\vec{M}$, enables determination of the induction vector $\vec{B}$ according to the equation $\vec{B}=4\pi\vec{M}+\vec{H}$.[31] Figure 7(a) shows the angle θ_B, between $\vec{B}$ and the *ab* plane, measured at 20 K, as a function of the external field H, applied at different angles θ_H. The low field data in this figure reveal the flux-trapping phenomenon: For $0^0<\theta_H\leq 11^0$, $\vec{B}$ is parallel to the *ab* plane, i.e., flux is trapped in this plane. As the external field increases, flux "leaves" the *ab* plane and rotates towards the direction of $\vec{H}$. Figure 7(a) also shows that the rotation begins at lower fields as the θ_H increases. For θ_H above 11° trapping in the *ab* plane is hardly observed; however, a clear flux rotation is still observed up to approximately $\theta_H=40°$.

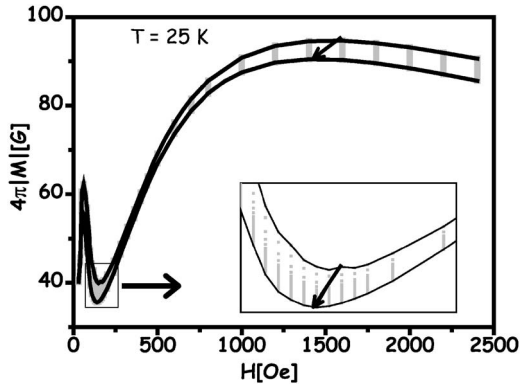

FIG. 6. Time dependence of the AMP demonstrating shift down of its onset and peak field with time.

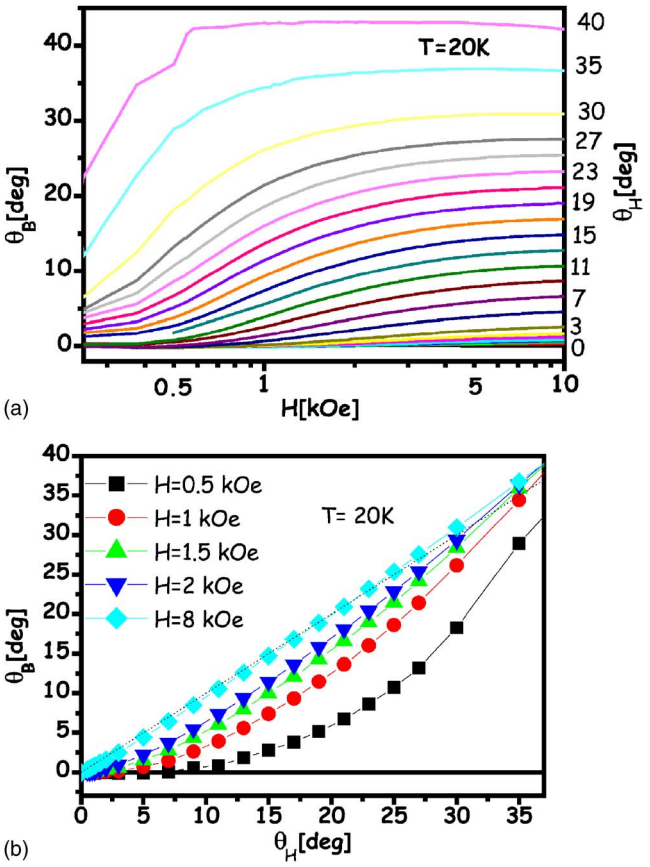

FIG. 7. (Color online) Illustration of flux trapping and rotation phenomena: (a) Angle θ_B, between $\vec{B}$ and the *ab* plane, measured at 20 K, as a function of the external field H, applied at different tilting angles θ_H. (b) θ_B as a function of θ_H for different fields.

The flux trapping, or "lock-in," phenomenon[16,21,25,26] is illustrated differently in Fig. 7(b), which shows θ_B as a function of θ_H for different fields. One can see that for $H=500$ Oe, $\theta_B=0$ up to a tilting angle $\theta_H\approx 8°$ of the external field. As the field increases and/or θ_H increases beyond 11°,

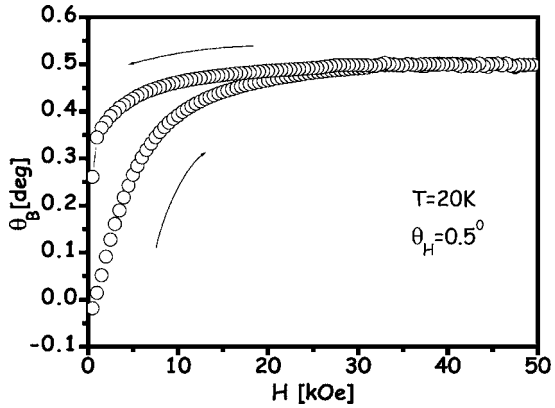

FIG. 8. Semiloop of θ_B versus H measured at 20 K in fields tilted at 0.5° to the *ab* plane. In the ascending branch, flux penetrates parallel to the *ab* plane and rotates towards the external field direction. In the descending branch only partial rotation back to the *ab* plane is observed.

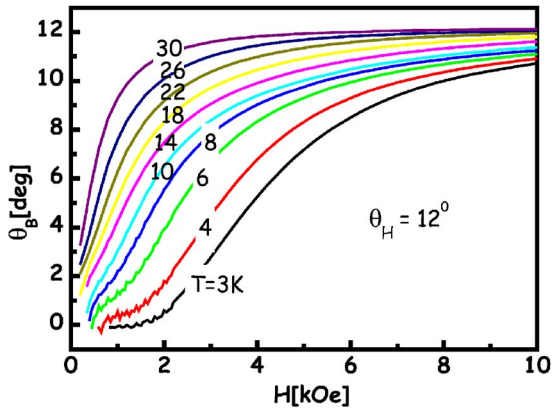

FIG. 9. (Color online) Temperature dependence of the flux rotation phenomenon illustrated in measurements of θ_B versus H at different temperatures, for fields applied at a constant tilting angle of 12°.

$\vec{B}$ rotates towards $\vec{H}$. For decreasing fields we observe flux rotation back towards the *ab* plane. However, on its way down the flux never reaches the *ab* plane. This is demonstrated in Fig. 8 showing a semiloop of θ_B versus H measured at 20 K in fields tilted at 0.5° to the *ab* plane. In the ascending branch, flux penetrates parallel to the *ab* plane and rotates towards the external field direction. However, in the descending branch only a partial rotation back to the *ab* plane is observed.

The temperature dependence of the flux rotation phenomenon is illustrated in Fig. 9, which shows θ_B versus H measured at different temperatures, for field applied at a constant tilting angle θ_H=12°. Figure 9 reveals a similar behavior as observed for the AMP (see Fig. 5), namely, with increasing temperature the rotation starts at lower fields. Flux creep also affects the flux rotation phenomenon. For a constant external field applied at a constant tilting angle, $\vec{B}$ rotates with time towards the direction of $\vec{H}$. This is illustrated in Fig. 10, which shows θ_B as a function of time for three different fields applied at an angle θ_H=10°. The data of Fig. 10 show a slow logarithmic increase of θ_B with time, indicating a creep of the direction of $\vec{B}$ towards the direction of $\vec{H}$.

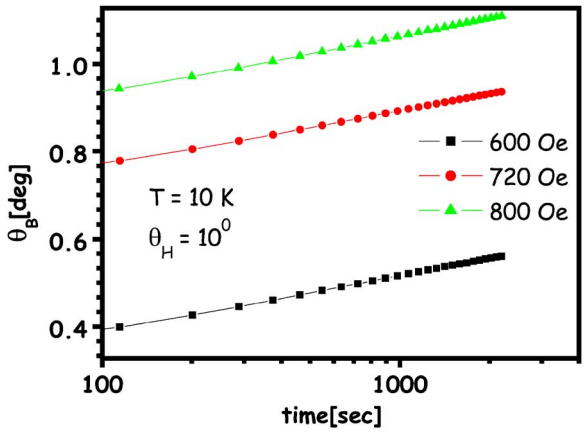

FIG. 10. (Color online) Time relaxation of the angle θ_B for three constant fields applied at an angle θ_H=10°.

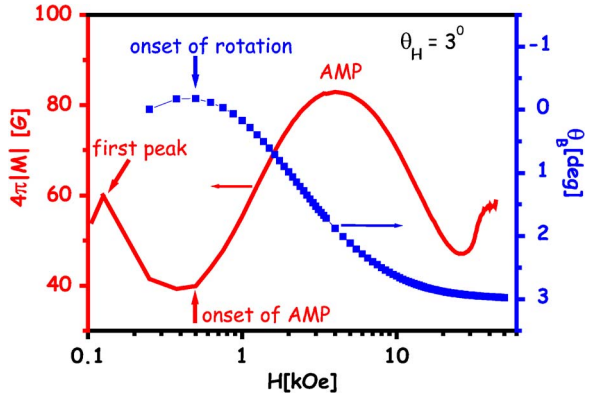

FIG. 11. (Color online) Comparison of the field dependence of M and θ_B, both measured in a field tilted at θ_H=3°. Arrows indicate the beginning of flux rotation and onset of the AMP.

IV. DISCUSSION

The experimental results described in the previous section point to a close relationship between the additional magnetization peak and the rotation of flux from the *ab* plane towards the field direction as the field increases. The correlation between these two phenomena is demonstrated in their field, tilting angle and temperature dependencies. Figure 11 compares the field dependence of M and θ_B, both measured in a field tilted at θ_H=3°. It is clearly seen that the onset of the AMP and the beginning of deviation of $\vec{B}$ from the *ab* plane occurs at the same field (about 500 Oe). Figure 12 compares the onset field of the AMP (circles) and the onset field of the flux rotation (triangles) for different tilting angles θ_H. The figure shows that the onset of flux rotation and the onset of the AMP follow a similar angular dependence up to $\theta_H \cong 11°$.[32] The peak occurs at much higher fields where the flux direction is almost parallel to the direction of $\vec{H}$. We also note that both the flux rotation angle and the AMP diminish as θ_H increases [see Figs. 4 and 7(a)]. In addition, when the field is swept down only a shallow AMP is observed (see Fig. 3) in agreement with the observation of partial flux rotation towards the *ab* plane (see Fig. 8). A correlation be-

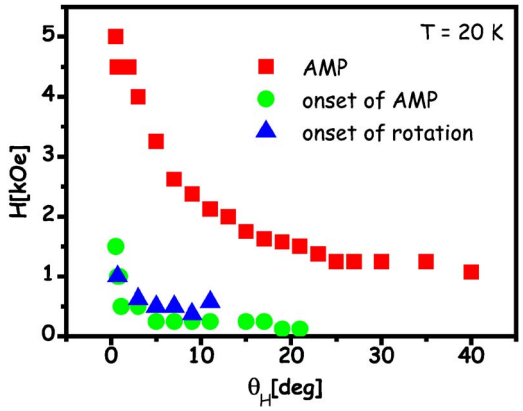

FIG. 12. (Color online) Measured onset field of the AMP (circles) and flux rotation (triangles) as a function of the tilting angles θ_H. The peak field is indicated by squares.

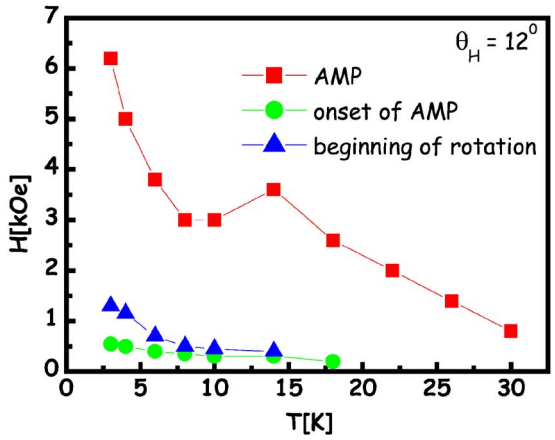

FIG. 13. (Color online) Temperature dependence of the onset field of the AMP (circles), the field corresponding to the beginning of flux rotation (triangles), and the peak field (squares), measured in fields tilted at $\theta_H = 12°$.

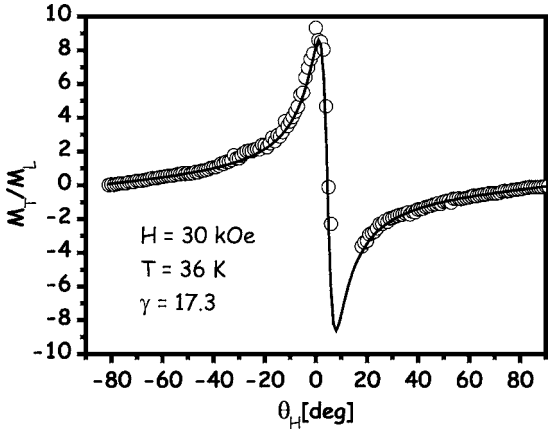

FIG. 14. Measured ratio M_T/M_L versus θ_H (circles) and theoretical fit (solid line) based on Eq. (1), yielding anisotropy ratio $\gamma = 17.3$.

tween flux rotation and the AMP is also observed in their temperature dependence. Figure 13 shows that in the temperature range (5–14 K) the onset field of the AMP (circles) and the field corresponding to the beginning of flux rotation (triangles) are close, both exhibiting a shift towards lower fields as temperature is increased. The peak occurs at much higher fields, exhibiting anomalous behavior around 15 K. This anomaly is related to the two-dimensional- (2D-) 3D transition in LSCO and will be discussed elsewhere.

Before discussing the physical origin of the relationship between the AMP and flux rotation phenomena, let us mention that both of these effects are obviously related to the crystal anisotropy. In order to determine the anisotropy ratio $\gamma = \sqrt{\frac{m_c}{m_{ab}}}$ in our crystal we employed the Kogan[14] formula for the ratio of the two components M_T and M_L of the vector $\vec{M}$ as a function of angle

$$\frac{M_T}{M_L} = (\gamma^2 - 1)\frac{\sin\theta_H \cos\theta_H}{\cos^2\theta_H + \gamma^2 \sin^2\theta_H}. \quad (1)$$

This formula has been successfully applied to $Bi_2Sr_2CaCu_2O_y$ and $YBa_2Cu_3O_{7-x}$ crystals yielding anisotropy ratios in accordance with values obtained using other methods.[4] As the validity of Eq. (1) is restricted only to the reversible regime, we measured M_T and M_L in our LSCO sample close to T_c ($T = 36$ K) and under a large external field of 30 kOe, as a function of the angle θ_H. The experimental data for the ratio M_T/M_L versus θ_H (circles) and the theoretical fit (solid line) based on Eq. (1), are shown in Fig. 14. This excellent one parameter fit yields $\gamma = 17.3$, in a good agreement with the value reported in the literature for optimally doped LSCO.[33] A similar value for the anisotropy ratio is obtained by employing the Blatter's *et al.*[20] scaling law, based on the 3D anisotropic Ginzburg-Landau theory, giving the angular dependence of the magnetization curve features

$$H_f(\theta_H) = H_f(0)(\sin^2\theta_H + \gamma^{-2}\cos^2\theta_H)^{-0.5}. \quad (2)$$

Equation (2) is based on the assumption that the difference in the direction between $\vec{B}$ and $\vec{H}$ is negligible, and thus it can be applied only in the high field regime, far above the AMP. We applied Eq. (2) to the field of the well-defined kink appearing in the SMP [see Fig. 2(b)]. Figure 15 shows the measured field of the kink as a function of the tilting angle (squares) together with the theoretical fit (solid line) based on Eq. (2). The fit yields $\gamma = 16.1$ in good agreement with the previous result. We note, however, that an attempt to apply this scaling law to the AMP data (circles) is less successful, as demonstrated in Fig. 15. The best fitting curve for the AMP (dashed line) yields an anisotropy ratio of 9.6, which is in variance with the established value of γ for LSCO samples. We conclude that the anisotropy of our LSCO sample is approximately 17 and that the 3D scaling law may be applied to predict the anisotropic behavior of certain magnetic features (e.g., the "kink" and the onset of the SMP). However, it is clear that the scaling law cannot predict the appearance of the additional magnetization peak in tilted fields, nor can it predict the flux rotation phenomena.

The relationship between the flux trapping and rotation phenomenon and the additional magnetization peak was first

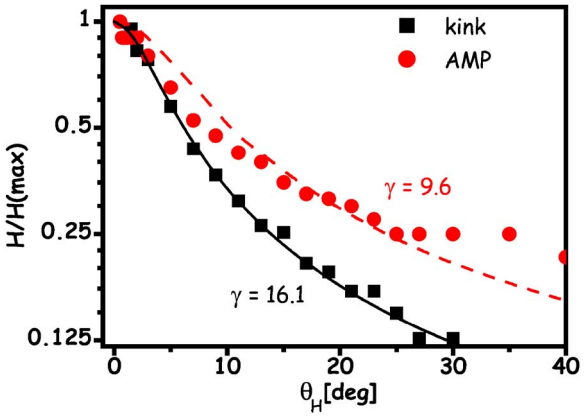

FIG. 15. (Color online) Measured field of the magnetization kink as a function of the tilting angle (squares) together with theoretical fit (solid line) based on Eq. (2). Dashed line demonstrates unsuccessful attempt to apply the scaling law to the AMP data (circles).

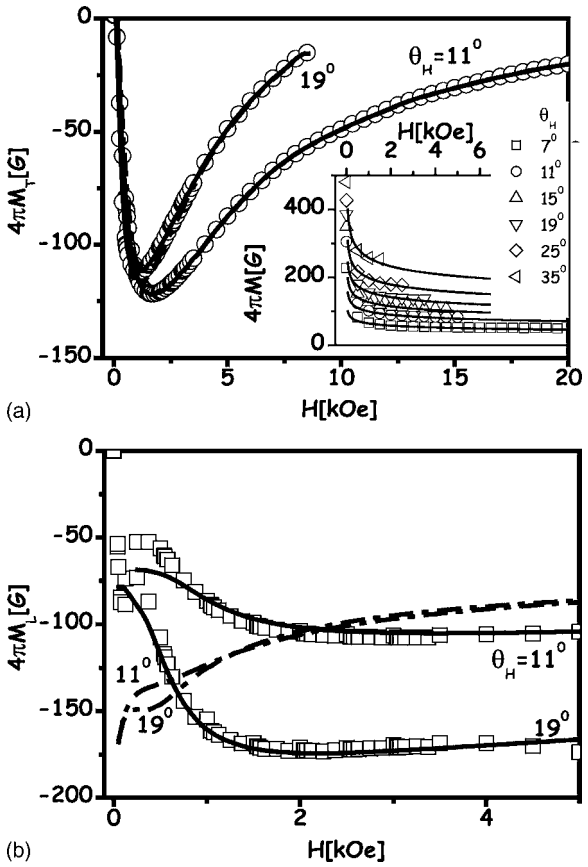

FIG. 16. Experimental data of (a) M_T vs H (circles) and (b) M_L vs H (squares) measured in fields tilted at $\theta_H=19°$ and $\theta_H=11°$. Dashed and solid curves are fits based on Eqs. (3) and (4), respectively. Dashed lines in are hardly distinguishable from the solid lines.

discussed by Bugoslavsky *et al.*[27] They attributed the peak rise to retardation of flux entry in the c direction due to flux trapping in the ab plane, and the peak fall to a subsequent flux entry in the c direction followed by the flux rotation towards the direction of the external field. We argue below that, in contrast to the Bugoslavsky *et al.*, flux trapping and rotation alone cannot fully explain the experimental data, and one must consider a tilt of the current flow plane associated with the flux rotation, which gives rise to a current enhancement. In order demonstrate our point we calculated M_T and M_L versus H, assuming flux trapping and rotation, with and without current enhancement, and compared the calculated results with the experimental data. The dashed lines in Figs. 16(a) and 16(b) show the calculated curves, assuming flux trapping and rotation alone, for fields tilted at angles 11° and 19° from the ab plane. These curves were calculated in the following way: the field dependence of the angle $(\theta_H-\theta_B)$ between $\vec{B}$ and $\vec{H}$ was taken from the experimental data described in Fig. 7. The intrinsic field dependence of M was determined from the descending branch of the hysteresis loops, where the AMP is absent. Theoretical fits yield $M \propto H^{-0.15}$ for a large range of tilting angles [see inset to Fig. 16(a)]. The magnitude of $\vec{B}$ was taken as the component of $(\vec{H}+4\pi\vec{M})$ along the $\vec{B}$ direction, i.e.,

$$B = H\cos(\theta_H-\theta_B) - C[H\cos(\theta_H-\theta_B)]^{-0.15}, \qquad (3)$$

where C is a fitting parameter. Knowledge of $\vec{B}$ and $\vec{H}$ allows calculation of $\vec{M}$, and thus M_T and M_L, for the measured $(\theta_H-\theta_B)$ as a function of H.

The calculated curves [dashed lines in Fig. 16(a), hardly distinguishable from the solid lines] yield excellent fit for the measured M_T (circles) using $C=300$ G. However, the calculated curves for M_L [dashed lines in Fig. 16(b)] show no resemblance to the experimental data (squares). In particular the calculated curves exhibit much narrower peaks and much lower onset fields than those observed experimentally, demonstrating that flux trapping and rotation alone cannot explain the data.

The data is well explained in our following approach which takes into account variations in $\vec{M}$ caused by a tilt of the current flow plane associated with the flux rotation. As a consequence of the anisotropic effective mass, currents have both "easy" and "hard" flow planes, parallel and perpendicular to the ab plane, respectively. Comparison of the hysteresis loops width presented in Figs. 2(a) indicates that current flowing in the "easy" plane (perpendicular to the c axis) creates larger magnetization than current flowing in the "hard" plane (perpendicular to the ab plane). Thus, a change of θ_B from 0° to θ_H with increasing field corresponds to a change of the current flow from a hard plane towards an easy plane, leading to an increase in M. On the other hand, the current and thus the magnetic moment intrinsically reduce as the field increases. A competition between these two effects creates a peak in the magnetization curve identified as the AMP. The solid lines in Figs. 16(a) and 16(b) were calculated following the same procedure leading to Eq. (3), however, we took into account an increase of the magnetization component along $\vec{B}$ by a factor $\varepsilon=\sqrt{[\cos(\theta_B)/\gamma]^2+\sin^2\theta_B}$, due to the current increase followed by an increase of θ_B. Namely, Eq. (3) was replaced by

$$B = H\cos(\theta_H-\theta_B) - \varepsilon C[\varepsilon H\cos(\theta_H-\theta_B)]^{-0.15}. \qquad (4)$$

Note that, in addition to the scaling of M, the field H was also scaled according to Eq. (2). The calculated curves [solid lines in Figs. 16(a) and 16(b)] yield excellent fit to the experimental data for *both* M_T and M_L using $C=1530$ G. Small deviations are observed only at low fields corresponding to very small θ_B, where the 3D scaling law [Eq. (2)] may not be applied because of possible formation of 'kinked' or crossed lattices vortex structures where Josephson vortices (JVs) are involved.

We finally note that anisotropic pinning effects may also contribute to the evolvement of the AMP. Assuming that for external field applied parallel to ab plane flux penetrates as JVs, the pinning force associated with them is very small as compared to Abrikosov vortices, since in JVs the order parameter has a finite value even at the core of the vortex. When flux rotates from the ab plane towards the field direction, kinked vortices or crossing lattices are generated, and the pinning force, and thus the critical current, increases due to the formation of Abrikosov pancakes. It should be noted, however, that JV exist only in the 2D regime were interac-

tion between CuO layers is weak and the anisotropy is sufficiently high. As LSCO has an intermediate anisotropy ($\gamma \approx 17$), it is not clear yet whether JV are altogether created in LSCO.

V. SUMMARY AND CONCLUSIONS

We demonstrated correlation between the additional magnetization peak and flux rotation in optimally doped LSCO under tilted fields. At low fields and angles close to the *ab* plane, the flux resides in the *ab* plane signifying the well-known "lock-in" phenomenon. As the field is increased, flux rotates towards the field direction, causing a tilt of the current flow plane towards an "easy" direction, namely, the *ab* plane. The AMP results from a competition between the current increase associated with this tilt and the intrinsic current decrease associated with the field increase. A theoretical simulation of this process yields excellent fit to the experimental data.

ACKNOWLEDGMENTS

This project was supported by the German-Israel Foundation (GIF), Israel Science Foundation (ISF)-Center of Excellence Program, and the Heinrich Hertz Minerva Center for High Temperature Superconductivity.

[1] D. E. Farrell, C. M. Williams, S. A. Wolf, N. P. Bansal, and V. G. Kogan, Phys. Rev. Lett. **61**, 2805 (1988).
[2] D. E. Farrell, J. P. Rice, D. M. Ginsberg, and J. Z. Liu, Phys. Rev. Lett. **64**, 1573 (1990).
[3] J. C. Martinez, S. H. Brongersma, A. Koshelev, B. Ivlev, P. H. Kes, R. P. Griessen, D. G. de Groot, Z. Tarnavski, and A. A. Menovsky, Phys. Rev. Lett. **69**, 2276 (1992).
[4] M. Tuominen, A. M. Goldman, Y. Z. Chang, and P. Z. Jiang, Phys. Rev. B **42**, 412 (1990).
[5] P. L. Gammel, D. J. Bishop, J. P. Rice, and D. M. Ginsberg, Phys. Rev. Lett. **68**, 3343 (1992).
[6] A. Grigorenko, S. Bending, T. Tamegai, S. Ooi, and M. Henini, Nature (London) **414**, 728 (2001).
[7] S. Ooi, T. Shibauchi, K. Itaka, N. Okuda, and T. Tamegai, Phys. Rev. B **63**, 020501(R) (2000).
[8] V. K. Vlasko-Vlasov, A. Koshelev, U. Welp, G. W. Crabtree, and K. Kadowaki, Phys. Rev. B **66**, 014523 (2002).
[9] M. Tokunaga, M. Kobayashi, Y. Tokunaga, and T. Tamegai, Phys. Rev. B **66**, 060507(R) (2002).
[10] M. Tokunaga, M. Kishi, N. Kameda, K. Itaka, and T. Tamegai, Phys. Rev. B **66**, 220501 (2002).
[11] A. Tonomura, H. Kasai, O. Kamimura, T. Matsuda, K. Harada, T. Yoshida, T. Akashi, J. Shimoyama, K. Kishio, T. Hanaguri, K. Kitazawa, T. Masui, S. Tajima, N. Koshizuka, P. L. Gammel, D. Bishop, M. Sasase, and S. Okayasu, Phys. Rev. Lett. **88**, 237001 (2002).
[12] S. Kasahara, Y. Tokunaga, N. Kameda, M. Tokunaga, and T. Tamegai, Phys. Rev. B **71**, 224505 (2005).
[13] A. N. Grigorenko, S. J. Bending, I. V. Grigorieva, A. E. Koshelev, T. Tamegai, and S. Ooi, Phys. Rev. Lett. **94**, 067001 (2005).
[14] V. G. Kogan, M. M. Fang, and S. Mitra, Phys. Rev. B **38**, 11958 (1988).
[15] P. H. Kes, J. Aarts, V. M. Vinokur, and C. J. van der Beek, Phys. Rev. Lett. **64**, 1063 (1990).
[16] D. Feinberg and C. Villard, Phys. Rev. Lett. **65**, 919 (1990).
[17] A. I. Buzdin and A. Simonov, Zh. Eksp. Teor. Fiz. **98**, 2074 (1990).
[18] S. Theodorakis, Phys. Rev. B **42**, 10 172 (1990).
[19] A. I. Buzdin and A. Simonov, Physica C **175**, 143 (1991).
[20] G. Blatter, V. B. Geshkenbein, and A. I. Larkin, Phys. Rev. Lett. **68**, 875 (1992).
[21] L. N. Bulaevskii, M. Ledvij, and V. G. Kogan, Phys. Rev. B **46**, 366 (1992).
[22] A. E. Koshelev, Phys. Rev. Lett. **83**, 187 (1999).
[23] A. E. Koshelev, Phys. Rev. B **71**, 174507 (2005).
[24] P. A. Mansky, P. M. Chaikin, and R. C. Haddon, Phys. Rev. Lett. **70**, 1323 (1993).
[25] V. Vulcanescu, G. Collin, H. Kojima, I. Tanaka, and L. Fruchter, Phys. Rev. B **50**, 4139 (1994).
[26] Y. V. Bugoslavsky, A. A. Zhukov, G. K. Perkins, A. D. Caplin, H. Kojima, and I. Tanaka, Phys. Rev. B **56**, 5610 (1997).
[27] Y. V. Bugoslavsky, A. L. Ivanov, V. A. Kovalsky, and A. A. Minakov, Physica C **257**, 284 (1996).
[28] T. Kimura, K. Kishio, T. Kobayashi, Y. Nakayama, N. Motohira, K. Kitazawa, and K. Yamafuji, Physica C **192**, 247 (1992).
[29] Zero-tilting angle was achieved by rotating the sample relative to the field direction in steps of 0.1° until the transverse component of the magnetization is diminished and the longitudinal component is minimum.
[30] Second magnetization peak appears only above 25 K in this field range.
[31] The demagnetization factor ~0.3 should be taken into account for accurate determination of $\vec{B}$. However, for most of the data the demagnetization correction is smaller than 10%.
[32] Above this angle the "lock-in" effect is not observed and thus, the onset of flux rotation is ill defined.
[33] T. Sasagawa, K. Kishio, Y. Togawa, J. Shimoyama, and K. Kitazawa, Phys. Rev. Lett. **80**, 4297 (1998).